

Numerical Simulation of Oxidation Effects in the Laser Cutting Process

Kai Chen, Y. Lawrence Yao and Vijay Modi

Department of Mechanical Engineering, Columbia University, New York, USA

A numerical model is developed for the process of oxygen-assisted laser cutting of mild steel. Coupled oxygen concentration and energy balance equations are solved by a control-volume-based computational scheme, while the velocity field is obtained by analytical boundary theory. The enthalpy method is adopted to trace the free boundary of the phase change and thus determine the molten-layer thickness. The steady-state simulation results include the temperature and oxygen concentration profiles at the cut front, the effects of impurity gas on the cutting speed, reaction energy, conduction loss and heat affected zone. The striation phenomenon is studied and the temperature fluctuation range versus cutting speed and oxygen pressure shows similar trends to the experimental results.

Keywords: Laser cutting; Oxidation; Striation

1. Introduction

Laser cutting is one of the most common manufacturing processes involving lasers and has made headway into well-established areas of manufacturing. Modelling of the laser cutting process has been addressed by many investigators to help understand the phenomena and basic mechanisms involved and to help predict the effects of process parameters. Owing to the complexity of the physical phenomena these modelling efforts are normally focused on particular aspects of the process under certain assumptions. For instance, most of the early modelling efforts used the energy balance, with heat conduction derived from the analytical solution of a moving heat source [1,2]. More involved models have been proposed by Modest and Abakians [3], Schulz et al. [4,5] and Cai and Sheng [6] where other effects such as phase change, kerf geometry and surface absorption were taken into account.

Most of the above models, however, pertain only to inert gas cutting, whereas in the majority of industrial practice, laser

cutting of mild steel uses oxygen as the assist gas to provide exothermic energy and to help increase cutting speed. In work that dealt with oxygen assisted cutting, a fixed percentage of material participating in the reaction was assumed [7], or small perturbation and simplified assumptions were used [8]. One important phenomenon in oxygen-assisted cutting is the formation of stria, which has received much attention since the early stage of laser cutting because it strongly affects the cut quality [9]. The explanations given for this phenomenon have been hydrodynamic instability [10], internal instability of the cutting process [8], cyclic oxidation [9,11], and, more recently, cyclic oxidation caused by hydrodynamic instability [12]. More quantitative and in-depth understanding as well as prediction capabilities can be achieved through numerical studies.

This paper presents an oxidation model based on heat transfer, transport and chemical rate theory. By solving the coupled energy and oxygen concentration equations, the model is capable of describing the details of the oxidation process and estimating the effects such as reaction energy, and oxygen purity on cutting speed. The energy balance equation is written in the form of enthalpy for the convenience of dealing with phase change and thus for determining the change of the molten layer thickness. The velocity field is obtained by balancing the shear stress at the interface. Both steady-state and transient behaviours are studied. In conjunction with the hydrodynamic instability analysis of the molten layer [12], temperature fluctuation caused by periodical removal of the molten layer is simulated and related to striation characteristics.

2. Theoretical Background

2.1 Physical Model

A simplified model is shown in Fig. 1. The workpiece is fed at a constant speed in a direction perpendicular to the laser beam. Laser irradiation together with the reaction energy heats up the metal, and the gas jet exerts momentum on the molten material, leading to the ejection of the melt. To obtain a realistic yet reasonable model, the following assumptions are made:

Correspondence and offprint requests to: Dr L. Yao, Department of Mechanical Engineering, Columbia University, 220 S.W. Mudd, Mail Code 4703, 500 West 120th Street, New York, NY 10027, USA. E-mail: yly1@columbia.edu

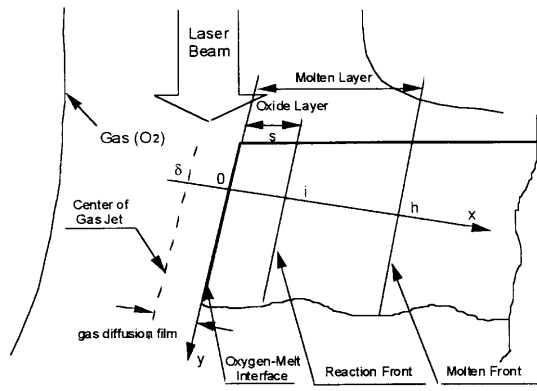


Fig. 1. Physical model.

1. The solid and liquid are isotropic with homogeneous properties.
2. The main mechanism of material removal is melting and the effect of vaporisation is neglected in this calculation. The measured molten front temperature in the continuous wave cutting process is well below the boiling temperature of mild steel [9,11], and thus evaporation plays a minor role in material removal.
3. The effect of plasma is not considered. While in laser welding or evaporative cutting of metals, the effect of the plasma plume above the cut front must not be neglected, this effect is negligible in continuous wave cutting because of the relatively lower front temperature and the strong gas jet which continuously dissipates the plume.
4. The radiative heat loss is neglected. It has been calculated by other published models that the surface losses are negligible [3].
5. The chemical reaction is of the heterogeneous type and takes place at a single planar interface.

The mass transfer in the oxidation process consists mainly of:

1. The mass transfer from the bulk gas phase to the melt surface (e.g. from $x = \delta$ to $x = 0$ in Fig. 1).
2. The mass transfer in the reacted layer (from $x = 0$ to $x = i$).
3. The first-order reaction at the reaction plane ($x = i$).

The reason for taking into account the presence of a gas diffusion film is that in almost all cases, the oxygen stream has some impurity, typically due to the presence of some inert gases. When the oxygen is consumed by the oxidation, the inert gases are left there and quickly build up into a boundary layer through which oxygen must diffuse to participate in the reaction. This makes the cutting process sensitive to even small levels of impurity in the oxygen jet [13]. The molten layer including the oxide layer is highly unstable under the high speed gas jet. It may rupture and grow cyclically [12], and the oxide, once formed, is highly resistive to oxygen diffusion. In our study, the simulation consists of two stages: the steady-state computation stage which also assumes that the reaction occurs at the gas-liquid interface without the formation of an oxide layer; and the time-dependent calculation stage which assumes that the growth of the oxide layer follows the well-

known parabolic law for diffusion-controlled reaction and that the oxide layer is subsequently removed by hydrodynamic forces. The input heat sources are the absorbed laser heat and the exothermic reaction heat. Heat is lost from the cutting zone by conduction, phase change and convection.

2.2 Governing Equations and Boundary Conditions

2.2.1 Mass Balance

The governing equation for mass transfer in the gas phase is (neglecting diffusion in the y -direction and convection in the x -direction, shown in Fig. 1):

$$c \frac{\partial X_{O_2}}{\partial t} + cv \frac{\partial X_{O_2}}{\partial y} = - \frac{\partial}{\partial x} N_{O_2} \quad (1)$$

where c is the molar density, X the gas concentration, v the gas velocity along the y -direction and N is the mass flux. The subscript O_2 denotes oxygen.

The oxygen diffusion consists of the molecular diffusion and the net bulk convection according to Fick's Law. Assuming that a small amount of impurity gas (e.g. nitrogen) exists, the molar flux of oxygen is expressed as:

$$N_{O_2} = - cD_{O_2,g} \frac{\partial X_{O_2}}{\partial x} + X_{O_2} (N_{O_2} + N_{N_2}) \quad (2)$$

where D is the diffusion coefficient and the subscripts N_2 and g denote nitrogen and gas phase, respectively.

It is reasonable to assume that no impurity gas enters the liquid oxide layer, thus $N_{N_2} = 0$, and Eq. (1) can be combined with Eq. (2) to yield:

$$c \frac{\partial X_{O_2}}{\partial t} + cv \frac{\partial X_{O_2}}{\partial y} = \frac{\partial}{\partial x} \left(\frac{cD_{O_2,g}}{1 - X_{O_2}} \frac{\partial X_{O_2}}{\partial x} \right) \quad (3)$$

In our transient calculation, a thin oxide layer with a large resistance is assumed to be present and the oxygen must diffuse through the liquid oxide layer before a chemical reaction takes place. The reaction is thus diffusion controlled and is largely dependent on the behaviour of the oxide layer. The governing equation for mass transfer in liquid phase oxide layer is:

$$c \frac{\partial X_{O_2}}{\partial t} + cv \frac{\partial X_{O_2}}{\partial y} = \frac{\partial}{\partial x} \left(cD_{O_2,m} \frac{\partial X_{O_2}}{\partial x} \right) \quad (4)$$

where the subscript m denotes the melt phase.

The boundary condition for the above described mass transfer is $X_{O_2} = X_{O_2,bulk}$ at the bulk gas stream. At the reaction front i in Fig. 1, a first-order chemical reaction leads to

$$N_{O_2} = k_r c (X_{O_2,i} - X_{O_2,e}) \quad (5)$$

where the subscripts i and e stand for reaction front and equilibrium state, and the kinetic rate k_r constant has an Arrhenius temperature dependence:

$$k_r = k_{r,0} \exp(-E_d/RT) \quad (6)$$

where k_{r0} is the kinetic rate constant, E_a the reaction energy, R the universal constant and T is the temperature.

The equilibrium concentration $X_{O_2,e}$ is obtained from the equilibrium constant K_e which is determined by Gibbs free energy of the reaction:



$$\Delta G_{rx}^o = -RT \ln K_e \quad (8)$$

where η is a reaction number and l and g denote liquid and gas states. The standard free energy for the above reaction is [14]:

$$\Delta G_{rx}^o = -56900 \text{ (cal)} + 11.82T \quad (9)$$

Owing to the non-stoichiometric nature of iron oxide, η is not a constant. It is taken to be one, since experimental observation reveals that FeO accounts for 97.6% of the oxides [15].

2.2.2 Energy Balance

The governing equation for heat transfer in the gas phase is in the parabolic form which is similar to the case of mass transfer:

$$\rho_g \frac{\partial c_p T}{\partial t} + \rho_g v \frac{\partial c_p T}{\partial y} = \frac{\partial}{\partial x} \left(K_g \frac{\partial T}{\partial x} \right) \quad (10)$$

where ρ , c_p , and K are density, heat capacity, and heat conductivity, respectively.

The equation for heat transfer, involving phase change in the material, can be expressed in the enthalpy formulation:

$$\frac{\partial \rho h}{\partial t} + \frac{\partial \rho \Delta H}{\partial t} + \frac{\partial \rho v h}{\partial y} + \frac{\partial \rho v \Delta H}{\partial x} = \frac{\partial}{\partial x} \left(K \frac{\partial T}{\partial x} \right) \quad (11)$$

where h is the sensible enthalpy defined as $h = h_{ref} \int_{T_{ref}}^T c_p dT$ and ΔH is the latent heat content. It either varies with h_m (latent heat) or is zero, depending upon whether the temperature exceeds the melting temperature. For simplification, it is assumed that the melting temperature is the melting point of pure iron (1527 °C). If phase change takes place over a temperature range, a liquid fraction is needed to account for this effect [16]. In our calculation, each grid during phase change is assumed to be in single phase (either liquid or solid).

The laser heat source can be described by a Gaussian distribution function given by

$$q_l = P_l \exp \left[-\left(\frac{r}{r_l} \right)^2 \right] \quad (12)$$

where P_l is the laser power density, r and r_l are the distances from the laser beam centre and the beam radius, respectively. The average laser power density can be calculated accordingly. The reaction heat source is obtained from:

$$q_r = 2\Delta H_R N_{O_2} \quad (13)$$

where ΔH_R is the reaction energy.

The boundary conditions for energy balance are that both the bulk gas temperature, and the solid temperature far away from heat sources, are equal to ambient temperature.

2.2.3 Momentum Balance

Instead of solving complex two-phase Navier–Stokes equations, the velocity field is assumed from boundary-layer theory. For the gas phase, the air velocity profile close to the liquid surface is assumed to be the same as that for turbulent flow in a smooth-walled channel. The seventh-power velocity-distribution law is adopted here [17].

$$\frac{v}{v^*} = 8.74 \left(\frac{-xyv^*}{\nu_g} \right)^{1/7} \quad (14)$$

where ν_g is the kinematic viscosity, and v^* is the friction velocity determined by

$$\frac{U}{v^*} = 8.74 \left(\frac{Hy^*}{2\nu_g} \right)^{1/7} \quad (15)$$

where U is the main stream gas velocity and H is the kerf width.

The velocity profile in the melt phase is assumed to be linear and the surface velocity V_s is determined by matching the shear stress across the interface,

$$\rho_g v^{*2} = \frac{\mu V_s}{h} \quad (16)$$

where μ is the viscosity of the melt and h is the thickness of the molten layer.

2.3 Physical Properties

Most of the physical properties are temperature dependent and must be updated during the calculation. The diffusivity of oxygen in the gas phase $D_{O_2,g}$ is not affected by concentration for low to moderate pressure (<10 atm). It is dependent on the absolute temperature (T), the pressure (P), the molecular weight (M) and the diffusion volume (V) of the impurity gas, and can be correlated as [18]:

$$D_{O_2,g} = \frac{0.001T^{1.75} \left(\frac{1}{M_{O_2}} + \frac{1}{M_{N_2}} \right)^{1/2}}{P(V_{O_2}^{1/3} + V_{N_2}^{1/3})^2} \quad (17)$$

The diffusivity of oxygen in the liquid (melt) phase takes the form of

$$D_{O_2,m} = D_{0,m} \exp(-E_d/RT) \quad (18)$$

The diffusivity of oxygen in liquid FeO is about $4 \times 10^{-4} \text{ cm}^{-2} \text{ s}^{-1}$ at 1550 °C. It may, however, reduce as the ferric iron concentration increases. The coefficient $D_{0,m}$ in Eq. (18) is determined so that the diffusivity matches the above value.

The molar density of the gas can be calculated from the ideal gas law:

$$c = \frac{P}{RT} \quad (19)$$

Few sources are available for the oxidation rate of pure iron. An approximate rate is inferred from the experimental results of Robertson and Jenkins [19]. The reaction controlled experiment was conducted by levitating a 1 g sphere iron in

an ample supply of oxygen. The rate corresponds to an oxidation flux of iron of $0.36 \text{ g}_{\text{Fe}} \text{ cm}^{-2} \text{ s}^{-1}$ at a temperature of $1600 \text{ }^\circ\text{C}$. The oxygen flux is thus about $0.10 \text{ g}_{\text{O}_2} \text{ cm}^{-2} \text{ s}^{-1}$ or $3.2 \times 10^{-3} \text{ mol cm}^{-2} \text{ s}^{-1}$. The equilibrium concentration can be neglected in this case and the kinetic rate constant is simply N_{O_2}/c , about $0.49 \times 10^3 \text{ cm s}^{-1}$.

The thermal conductivity of oxygen is correlated as [20]:

$$K_g = 0.024 \left(\frac{T}{273} \right)^{1.5} \left(\frac{273 + 240}{T + 240} \right) \quad (20)$$

Thermal conductivity of liquid metals is related to the electrical conductivity at high temperature as [21]:

$$K_m = 2.45 \times 10^{-8} \frac{T}{\rho_e} \quad (21)$$

$$\rho_e = 1.54 \times 10^{-4} T + 1.081 [\mu\Omega\text{m}] \quad (22)$$

The absorption distribution of the laser power for different cutting front geometry has been studied by Petring et al [22]. For the TEM_{00} mode and a circular polarised laser beam, the absorption coefficient is about 30% for inclination between 80° and 88° , but reduces to about 10% when the inclination increases to 90° . Here, a constant of 30% is used for calculation. The heat of reaction is taken to be $\Delta H_r = -257.58 \text{ kJ mol}^{-1}$ (of iron).

2.4 Numerical Scheme

A typical computational grid layout is shown in Fig. 2. A control-volume based discretisation method is used to solve the coupled convection–diffusion problem. A detailed description of discretisation of the parabolic governing equation is given by Patankar [23]. The 2D discretisation equations are written in the fully implicit forms. The coefficients of the discretisation equations are associated with the local convection and conductance and must be interpolated between the values of grid points. A power-law scheme is used here, which provides a good representation of the convection–diffusion behaviour. The source term also includes values of the previous time step if the calculation is time dependent. The temperature- or concentration-dependent coefficients are linearised for each time-step

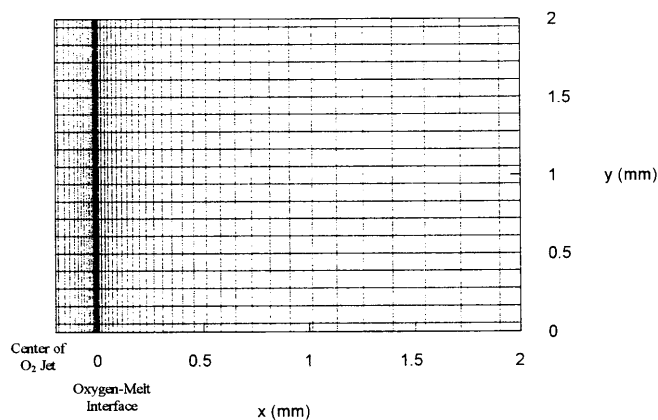


Fig. 2. A typical computational grid layout.

to facilitate the convergence. The discretisation equation groups are solved by a line-by-line tridiagonal matrix algorithm.

In our preliminary calculation, the variation of temperature and oxygen concentration at the gas–liquid interface was found to be insignificant along the direction of workpiece depth for thin workpieces (2 mm for our calculation). This was also confirmed by other researchers who found that the heat loss at the top and bottom surfaces owing to convection and radiation was negligible even in the presence of a strong gas jet [3]. It has been reported that the 2 mm thickness corresponds to a critical thickness beyond which two different patterns of striation are observed on the cut surface [11]. For simplification, the top and bottom boundaries of the calculation domain are assumed to be under insulation conditions. Thus, the 2D calculation is equivalent to that of a 1D calculation. All the results shown in this paper are of one dimension in the direction perpendicular to the gas–liquid interface. The 2D calculation scheme, however, has set the stage for a fully 2D extension which is currently under way, and which takes into account the effects of the molten front geometry. For this study, the incoming laser heat is assumed to be focused down to a point and is applied directly in the direction mentioned above. A laser heat flux of $1.2 \times 10^8 \text{ W m}^{-2}$ is used in the computation. Oxygen purity varies from 1 to 0.9, pressure from 2 to 3 bars, and cutting speed from 20 to 55 mm s^{-1} in the computation. The workpiece thickness is assumed to be 2 mm and the type of purity investigated includes nitrogen and helium.

3. Results and Discussions

3.1 Steady State Results

Figures 3(a) and 3(b) show the temperature profile with different oxygen purities, and gas pressures, respectively. As mentioned earlier, reaction is assumed to take place at the gas–liquid interface for the steady-state calculation, and the temperature is therefore highest at the interface. The temperature profile increases with both oxygen purity and gas pressure because of the more reactive energy generated at higher oxygen purity and gas pressure. The temperature quickly drops to the ambient level at the centre of the gas stream because of the large diffusion effect due to the temperature dependent heat conductivity. Inside the material, the temperature profile has a lower gradient and the heat affected zone (HAZ) can be estimated accordingly. If the HAZ is taken to be the region above $800 \text{ }^\circ\text{C}$, which corresponds to the transitional temperature of the microstructure of mild steel, the HAZ is about 0.7 mm from the interface for the parameters used in the calculation. The actual HAZ is the difference between this value and the molten-layer thickness.

Figure 4(a) shows the profile of oxygen concentration with different oxygen purities. A small decrease of purity brings about a large drop of oxygen concentration at the interface, thus greatly reducing the reaction energy that could be produced because the impurity quickly increases the resistance to further oxygen diffusion when oxygen is being consumed as mentioned early. It should be pointed out that if the convective term in Eq.(3) is neglected, the equation can be integrated as

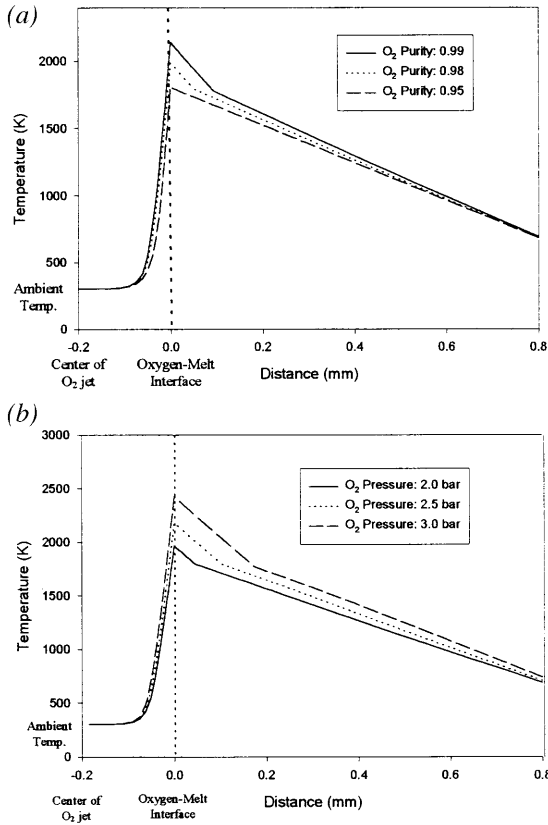


Fig. 3. (a) The temperature profile with different oxygen purities. (Laser heat flux = $1.2 \times 10^8 \text{ W m}^{-2}$, oxygen pressure = 2.5 bar, cutting speed = 45 mm s^{-1} .) (b) The temperature profile with different gas pressure. (Laser heat flux = $1.2 \times 10^8 \text{ W m}^{-2}$, oxygen purity = 0.99, cutting speed = 45 mm s^{-1} .)

$$N_{O_2,0} = \frac{cD_{O_2,g}(X_{N_2,0} - X_{N_2,\delta})}{X_{N_2,LM}\delta} \quad (23)$$

where 0 and δ denote locations shown in Fig. 1, and $X_{N_2,LM}$ is the logarithmic mean concentration and is defined as:

$$X_{N_2,LM} = \frac{(X_{N_2,0} - X_{N_2,\delta})}{\ln \frac{X_{N_2,0}}{X_{N_2,\delta}}} \quad (24)$$

The “net bulk flow” effect, represented by the logarithmic mean $X_{N_2,LM}$, increases rapidly as the concentration of the diffusing species approaches unity. This explains the rapid decrease of oxidation energy when oxygen is contaminated by a small amount of inert gas. The numerical results including the convective term in Eq. (3) show the same effect. Figure 4(b) shows the profile of oxygen concentration with different gas pressures. As seen, the concentration profile is insensitive to gas pressure. This is understandable because the kinetic rate and equilibrium concentration are all dependent on temperature and are not directly related to gas pressure.

Figure 5 shows the effects of oxygen purity on cutting speed. As seen, the cutting speed is highly sensitive to small levels of contamination in the oxygen jet, which is consistent with the experimental results given by Powell et al [13]. This

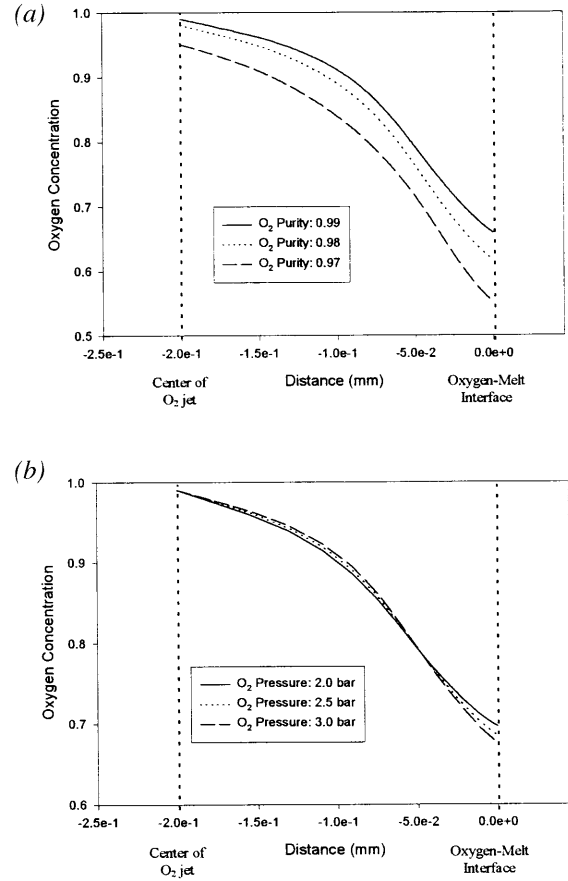


Fig. 4. (a) The oxygen concentration profile with different oxygen purities. (Laser heat flux = $1.2 \times 10^8 \text{ W m}^{-2}$, oxygen pressure = 2.5 bar, cutting speed = 45 mm s^{-1} .) (b) The oxygen concentration profile with different gas pressure. (Laser heat flux = $1.2 \times 10^8 \text{ W m}^{-2}$, oxygen purity = 0.99, cutting speed = 45 mm s^{-1} .)

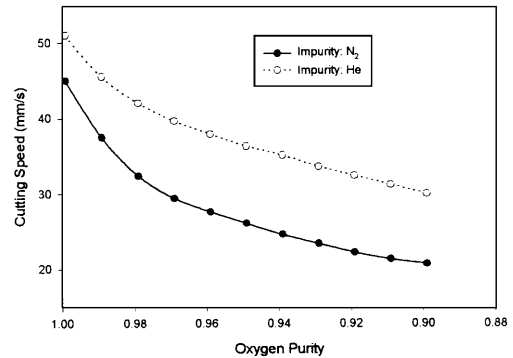


Fig. 5. The effects of oxygen purity and impurity type on cutting speeds. (Laser heat flux = $1.2 \times 10^8 \text{ W m}^{-2}$, pressure = 2.5 bar.)

sensitivity comes from the quickly accumulated gas diffusion film when the oxygen impurity increases, as mentioned earlier. The effects of various gaseous impurities are also shown in Fig. 5. The impurity He has less effect than N₂ because its smaller molecular weight and diffusion volume result in a larger diffusion coefficient (refer to Eq. (17)), and consequently

more oxygen flux for reaction, which is confirmed by experimental observation [24].

The calculated reaction heat, absorbed laser heat and conduction loss into the solid versus cutting speed are shown in Fig. 6. The laser heat input was calibrated so that the calculated interface temperature matches the empirical relationship between cutting speed and interface temperature [9]. As a consequence of the increasing interface temperature with the increasing cutting speed, the reaction heat and conduction loss also increase. At lower speeds, the reaction energy contributes nearly half of the total energy input and the heat conduction loss takes about half of the total heat loss, which agrees with the results of other researchers [5,25]. At higher speeds, the laser beam has better coupling at the molten front, therefore its relative contribution towards total energy input increases.

3.2 Striation Formation

In oxygen-assisted laser cutting of mild steel, a regularly spaced pattern known as striation is routinely observed on the cut surface. A commonly accepted explanation is that the striation is formed from cycles of ignition, burning and extinction [9,11]. It is further pointed out that striation formation is associated with the oxide layer which is hydrodynamically unstable under the gas jet [12]. Since the diffusivity of the oxides is much larger than that of the gas (about 10^4 times higher), the formation of an oxide layer severely hinders the oxidation process. However, the oxide layer is unstable and will rupture or become wavy under the hydrodynamic forces of the gas jet. The cyclic growth and removal of the oxide layer causes fluctuation of temperature and molten layer thickness, which causes the striation patterns.

Since the exact behaviour of the oxide layer under the effect of melt ejection is not well understood, a reasonable assumption is that the growth of the oxide layer for the diffusion controlled process follows the well-known parabolic law:

$$\frac{ds}{dt} = BD \frac{\partial c}{\partial x} \tag{25}$$

where s is the thickness of the oxide layer, D is the diffusion coefficient and B is a constant. The process is then simplified

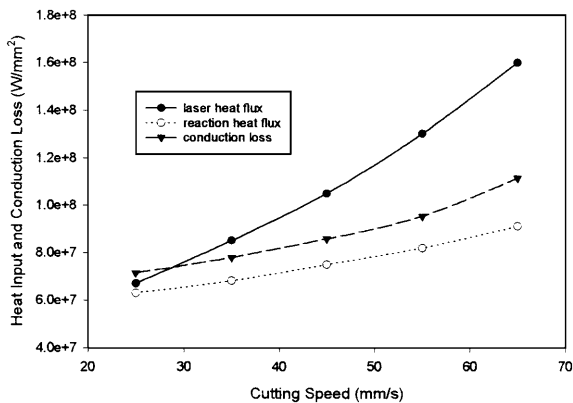


Fig. 6. Heat input and loss vs. cutting speed. (Oxygen purity = 0.995, pressure = 2.5 bar, interface temperature = 2200K.)

to a quasi-steady-state process so that the concentration on the oxide surface is independent of the oxide film, that is:

$$\frac{ds}{dt} = BD \frac{c_0 - c_i}{s(t)} \approx BD \frac{c_0}{s(t)} \tag{26}$$

where subscript 0 denotes the interface of oxide and oxygen and i the interface of metal and oxide (Fig. 1). The term c_i is near zero owing to consumption of oxygen at the reaction front i . The diffusion coefficient D and oxygen density c_0 are both temperature dependent, and can be combined into an exponential factor of temperature and a coefficient $A(P)$ which presumably has a linear relation with oxygen pressure P .

$$\frac{ds}{dt} = A(P) \frac{\exp(-T_0/T)}{s(t)} \tag{27}$$

The equation is then integrated to obtain the growth of the oxide layer.

The removal of the oxide layer under hydrodynamic instability is also a complicated process and its detailed, quantitative prediction is beyond the scope of this paper. We assume the process happens in a short time so that once the oxide layer grows to a certain point, the oxide layer is suddenly removed. After it is removed, the oxide layer starts to grow again. The period of this growth-removal cycle is obtained from the instability theory [12], which correlates reasonably with experimental results. Figure 7 shows typical cycles of front temperature fluctuation. The coefficient of the parabolic growth ($A(P)$ in Eq. (27) is not readily available and therefore it is calibrated so that the temperature fluctuation is around a level obtained from experiments [9]. When the oxide layer starts to grow, the oxidation slows down because of the high resistance of the oxide layer to the oxygen diffusion, and the temperature starts to drop. Once the oxide layer is removed, the temperature quickly picks up owing to a sudden increase of oxygen flux and reaction energy. This type of temperature fluctuation during the cutting process has been recorded via the light intensity change picked up by high-speed photography [9,26].

The temperature fluctuation is also inherently linked to molten-layer fluctuation, since the phase change produces a heat sink in the process. As shown in Fig. 8, the calculated molten-layer fluctuation caused by the temperature fluctuation shows a similar pattern to the experimental observation of the

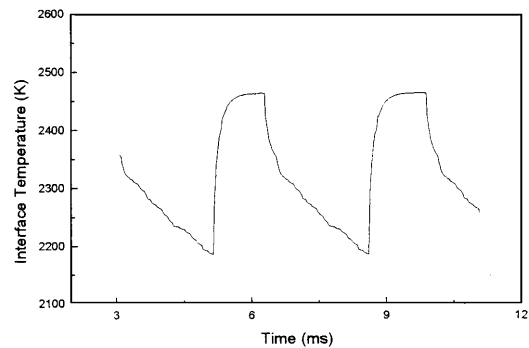


Fig. 7. The temperature fluctuation at the oxygen-melt interface. (Laser heat flux = 1.2×10^8 W m⁻², pressure = 2.5 bar, cutting speed = 35 mm s⁻¹.)

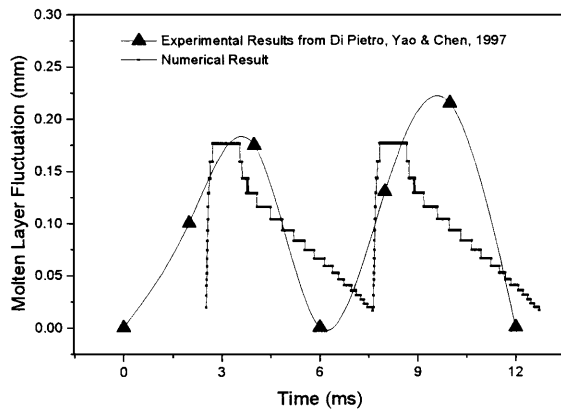


Fig. 8. Molten-layer fluctuation. (Laser heat flux = $1.2 \times 10^8 \text{ W m}^{-2}$, pressure = 2.5 bar, cutting speed = 25 mm s^{-1} .)

cut front mobility captured by the high-speed photography. Since, in our calculation, the thickness of the molten layer is obtained by summation of the grids where phase change takes place, the accuracy is limited by the grid size and the calculated thickness is somewhat stepwise. Given the limited resolution of the high-speed photography, the discrepancy between the experimental and numerical results is considered acceptable.

Figure 9 shows that the range of temperature fluctuation decreases with the increase of the cutting speed, so does striation depth, which is experimentally measured. It is known that the striation frequency increases with cutting speed. The higher frequency allows less time for the temperature to fluctuate, therefore the range of fluctuation decreases as the cutting speed increases. At the same time, reduced range of temperature fluctuation results in reduced striation depth. The gas pressure also has significant influence on the front temperature. When gas pressure increases, so does the molar density of the oxygen, resulting in increased oxygen flux and thus enhancing the reaction. Figure 10 shows the range of temperature fluctuation range versus pressure. The increase of pressure brings about the increase of temperature fluctuation range, which corresponds to increase of striation depth experimentally measured.

The striation formation is a complicated phenomenon which involves heat transfer, chemical reaction and hydrodynamic instability, and its full description requires more detailed effort.

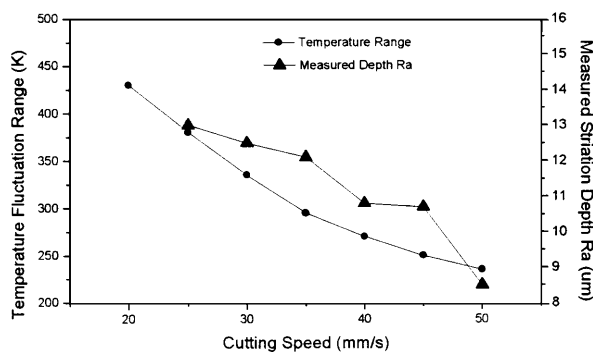


Fig. 9. Temperature fluctuation range and measured striation depth vs. cutting speed. (Laser heat flux = $1.2 \times 10^8 \text{ W m}^{-2}$, pressure = 2.5 bar.)

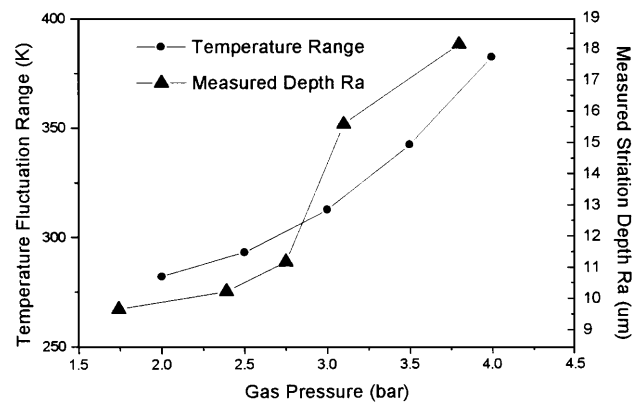


Fig. 10. Temperature fluctuation range and measured striation depth vs. gas pressure. (Laser heat flux = $1.2 \times 10^8 \text{ W m}^{-2}$, cutting speed = 35 mm s^{-1} .)

Our approach of combining numerical simulation with analytical instability analysis [12] captures the basic behaviour of the phenomenon and helps to quantify the formation process.

4. Concluding Remarks

The model developed in this paper describes the process of the oxygen-assisted cutting of mild steel and the numerical simulation quantitatively predicts the effects of oxidation. The numerical results show that the transport phenomenon in the gas stream cannot be neglected and thus explains why a small amount of oxygen impurity will greatly reduce cutting speed. The results also show that the parabolic growth law and the quasi-static treatment of the diffusion controlled process yield reasonable results. Other quantities such as reaction energy, heat conduction loss, and heat affected zone can be predicted by this model. The formation of striation is related to the unstable behaviour of the oxide layer since the oxidation energy is very sensitive of the oxide layer which has a large resistance to the diffusivity. With the oxide layer oscillation based on the instability theory, the striation phenomenon is simulated via transient temperature fluctuation and the molten-layer fluctuation. The trends of the temperature fluctuation range versus cutting speed and the gas pressure are consistent with the experimental results.

Acknowledgements

This work is supported by a NSF grant (DMI-9500181). Helpful discussion with Professor Nick Themelis is also gratefully acknowledged.

References

1. D. Schuocker and W. Abel, "Material removal mechanism of laser cutting", Proc. of SPIE, Vol. 455, Sept 26–27, 1983.
2. G. Chryssoulouris, J. Bredt, S. Kordas and E. Wilson, "Theoretical aspects of a laser machine tool", Journal of Engineering for Industry, 110, pp. 65–70, 1988.

3. M. F. Modest and H. Abakians, "Evaporative cutting of a semi-infinite body with a moving CW laser", ASME Journal of Heat Transfer, 108, pp. 602–607, 1986.
4. W. Schulz, G. Simon, H. M. Urbassek and I. Decker, "On laser fusion cutting of metals", Journal of Physics D: Applied Physics, 20, pp. 481–488, 1987.
5. W. Schulz, D. Becker, J. Franke, R. Kemmerling and G. Herziger, "Heat conduction losses in laser cutting of metals", Journal of Physics D: Applied Physics, 26, pp. 1357–1363, 1993.
6. L. Cai and P. Sheng, "Analysis of laser evaporative and fusion cutting", Journal of Manufacturing Science and Engineering, 118, pp. 225–234, 1996.
7. P. Di Pietro and Y. L. Yao, "A numerical investigation into cutting front mobility in CO₂ laser cutting", International Journal of Machine Tools and Manufacture, 35(5), pp. 673–688, 1995.
8. D. Schuocker, "Dynamic phenomena in laser cutting and cut quality", Applied Physics B, 40, pp. 9–14, 1986.
9. Y. Arata, H. Maruo, I. Miyamoto and S. Takeuchi, "Dynamic behavior in laser gas cutting of mild steel", Transactions JWRI, 8(2), pp. 15–26, 1979.
10. M. Vicaneek, G. Simon, H. M. Urbassek and I. Decker, "Hydrodynamic instability of melt flow in laser cutting", Journal of Physics D: Applied Physics, 20, pp. 140–145, 1986.
11. A. Ivarson, J. Powell, J. Kamalu and C. Magnusson, "The oxidation dynamics of laser cutting of mild steel and the generation of striations on the cut edge", Journal of Materials Processing Technology, 40, pp. 359–374, 1994.
12. K. Chen and Y. L. Yao, "Striation formation and surface finish in laser cutting of mild steels", Manufacturing Science and Technology, ASME MED-6-1, pp. 301–307, 1997.
13. J. Powell, A. Ivarson, J. Kamalu, G. Broden and C. Magnusson, "The role of oxygen purity in laser cutting of mild steel", ICALEO '92, pp. 433–442, 1992.
14. J. F. Elliott, Thermochemistry for Steelmaking, vol. 2, Addison-Wesley, 1963.
15. A. Ivarson, J. Powell and C. Magnusson, "Laser cutting of steels: a physical and chemical analysis of the particles ejected during cutting", Welding in the World, 30(5/6), pp. 116–125, 1992.
16. V. R. Voller and C. Prakash, "A fixed grid numerical modeling methodology for convection–diffusion mushy region phase-change problems", International Journal of Heat Mass Transfer, 30(8), pp. 140–145, 1987.
17. H. Schlichting, Boundary-Layer Theory, McGraw-Hill, New York, 1979.
18. N. J. Themelis, Transport and Chemical Rate Phenomena, Gordon and Breach, 1995.
19. D. G. C. Robertson and A. E. Jenkins, in G. R. Beltona and W. L. Worrel (ed.), Heterogeneous Kinetics at Elevated Temperatures, Plenum Press, New York, 1970.
20. F. M. White, Viscous Fluid Flow, McGraw-Hill, New York, 1991.
21. T. Iida and R. Guthrie, The Physical Properties of Liquid Metals, Oxford University Press, 1988.
22. D. Petring, P. Abels and E. Beyer, "Absorption distribution on idealized cutting front geometry and its significance for laser beam cutting", SPIE, 1020, High Power CO₂ Laser Systems and Applications, pp. 123–131, 1988.
23. S. V. Patankar, Numerical Heat Transfer and Fluid Flow, Taylor and Francis, 1980.
24. J. T. Gabzdyl and D. A. Morgan, "Assist gas for laser cutting of Steels", ICALEO '92, pp. 443–448, 1992.
25. M. Vicaneek and G. Simon, "Momentum and heat transfer of an inert gas jet to the melt in laser cutting", Journal of Physics D: Applied Physics, 20, pp. 1191–1196, 1987.
26. P. Di Pietro, Y. L. Yao and K. Chen, "An experimental study of on-line estimation of striations in laser cutting process", Technical Papers of NAMRI, pp. 105–110, 1997.

Nomenclature

B	constant in Eq. (25)
c	molar density
c_p	heat capacity
$D, D_{O_2,g}, D_{O_2,m}$	diffusion coefficient, diffusion coefficient of oxygen in gas and melt phases
$D_{0,m}$	diffusion constant
E_a	reaction energy
H	kerf width
h	thickness of molten layer or sensible enthalpy
h_m	latent heat
K, K_g, K_m	thermal conductivity, thermal conductivity in gas and melt phases
K_e	equilibrium constant
k_r	kinetic rate coefficient
$k_{r,0}$	kinetic rate constant
L	material thickness
M, M_{O_2}, M_{N_2}	molecular weight, and molecular weight of oxygen and nitrogen
N, N_{O_2}, N_{N_2}	mass flux, mass flux of oxygen and nitrogen
P	gas pressure
P_l	laser power density
q_l	laser heat flux
q_r	reaction heat flux
R	universal gas constant
r	distance from beam centre
r_l	radius of laser beam
s	thickness of the oxide layer
T	temperature
t	time
T_0	reaction temperature
T_m	melting temperature
U	bulk gas velocity
u	cutting speed
v^*	friction velocity
V, V_{O_2}, V_{N_2}	diffusion volume, diffusion volume of oxygen and nitrogen
v	velocity in y-direction
V_s	surface velocity
x	distance perpendicular to melt flow
$X_{N_2,LM}$	logarithmic mean concentration
$X_{N_2,0}, X_{N_2,\delta}$	nitrogen concentration at planes 0 and δ (Fig. 1)
$X_{O_2}, X_{O_2,i}, X_{O_2,e}$	oxygen concentration at the reaction plane i (Fig. 1) and equilibrium state
y	distance along melt flow
ρ, ρ_g	density, density in gas phase
ρ_e	electrical conductivity
ν, ν_g	kinematic viscosity, kinematic viscosity in gas phase
δ	thickness of gas diffusion film
μ	viscosity of melt
ΔG_{rx}	standard Gibbs free energy
ΔH	latent heat content
ΔH_R	reaction energy